Cluster glass transition and relaxation in the random spinel $CoGa_2O_4$

T. Naka,[1,*] T. Nakane,[1] S. Ishii,[2] M. Nakayama,[1] A. Ohmura,[3] F. Ishikawa,[3] A. de Visser,[4] H. Abe,[5] and T. Uchikoshi[1]

[1]*National Institute for Materials Science, 1-2-1, Sengen, Tsukuba, Ibaraki 305-0047, Japan*

[2]*Department of Physics, Tokyo Denki University, Hatoyama, Saitama 350-0394, Japan*

[3]*Faculty of Science, Niigata University, Niigata, 950-2181, Japan*

[4]*Van der Waals–Zeeman Institute, Institute of Physics, University of Amsterdam, Science Park 904, 1098 XH, Netherlands*

[5]*Joint and Welding Research Institution, Osaka University, 11-1 Mihogaoka, Ibaraki, Osaka 567-0047, Japan*

(Received 28 October 2020; accepted 25 May 2021; published 4 June 2021; corrected 18 February 2022)

We report magnetic properties in the random spinel magnet $CoGa_2O_4$. Rietveld analysis of the x-ray diffraction profile for $CoGa_2O_4$ reveals that the Co and Ga ions are distributed randomly in the tetrahedral A sites and octahedral B sites in the cubic spinel structure. $CoGa_2O_4$ exhibits a spin-glass transition at $T_{SG} = 8.2$ K that is confirmed by measurements of the dc and ac susceptibilities and thermoremanent magnetization (TRM) that develops below T_{SG}. From the frequency dependence of the freezing temperature T_f for $CoGa_2O_4$, it is indicated that the relaxation time $\tau(T)$ follows a Vogel-Fulcher law $\tau = \tau_0 \exp[-E_a/k_B(T - T_0)]$. An analysis of specific heat suggested that a doublet ground state of the octahedrally coordinated Co^{2+} was stabilized by spin-orbit and crystal field couplings. The relaxation rate of TRM is considerably enhanced at T_{SG} and decays rapidly above and below T_{SG}. The time course of TRM is reproduced by nonexponential relaxation forms, such as a stretched exponential (Kohlrausch) as well as Ogielski and Weron relaxation forms. This behavior is displayed universally in glass systems, and the characteristic parameters associated with these functions were reasonable.

DOI: 10.1103/PhysRevB.103.224408

I. INTRODUCTION

The A-site spinel antiferromagnets (AFMs) with stoichiometry AB_2O_4, where A is a divalent magnetic cation and B is a trivalent nonmagnetic cation, have been a platform for the realization of novel magnetic states (e.g., quantum spin or orbital liquid states [1–3]), pressure-induced valence transitions [4,5], and a Néel to spin spiral (NSS) transition [2], which is characterized by a propagation vector $\boldsymbol{q}$ that forms continuous surfaces in k space. In the spinel structure, the A and B cations occupy tetrahedral and octahedral sites, respectively. The former (latter) has previously been called the A site (B site). Actually, the A site forms a diamond lattice, which consists of two interpenetrated face-centered cubic (fcc) lattices shifted along the [111] axis. The A-site spinel is therefore magnetically bipartite. In other words, the Néel state is realized if one introduces only a nearest neighbor antiferromagnetic interaction J_1 between spins occupying sites in the respective fcc sublattices. As indicated in Fig. 1(a), a next-nearest neighbor antiferromagnetic interaction J_2 acts competitively with the nearest neighbor interaction, and a magnetic frustration effect is therefore anticipated. For such A-site frustrated antiferromagnets, a Monte Carlo simulation shows a distinctive phase diagram in the temperature-(J_2/J_1) plane. The simulation predicts that the Néel state is destabilized rapidly with increasing J_2/J_1 and that a magnetic transition to a spin spiral state occurs at $J_2/J_1 = 1/8$; meanwhile, densely quasidegenerated magnetic states characterized by propagation vector $\boldsymbol{q}$ form continuous surfaces in k space for $J_2/J_1 > 1/8$ [Fig. 1(b)] [2]. In the typical exemplary system, $CoAl_2O_4$ is expected to be a platform that exhibits novel magnetic behavior. Because "frustration" is an inherent topological feature of the A-site spinel or diamond lattice AFMs, the magnetic states are quite sensitive to crystallographic perturbations such as inversion [6,7], magnetic dilution [8], and chemical and physical pressures [8,9]. The inversion, which is a chemical disorder (antisite defect of cationic configuration between the A sites and B sites), is represented by the chemical formula $(A_{1-\eta}B_\eta)[B_{2-\eta}A_\eta]O_4$. In this representation, parentheses and square brackets indicate the A-site and B-site occupations, respectively, and η is the so-called inversion parameter. Microscopically, an inverted Co^{2+} ion at the B site couples strongly with neighboring Co^{2+} ions at the A site and B site via exchange interactions J_{AB} and J_{BB}, respectively [Fig. 1(a)].One can deduce therefore that these exchange interactions are spatially and randomly distributed in the A-site spinel and bring an exchange disorder, which seems to act as strong magnetic perturbations to the magnetic state, in particular, lifting the degeneracy due to the frustration and stimulating an ordering transition [10]. It has been revealed experimentally that a Néel to spin glass (NSG) transition occurs at $\eta_c \sim 0.08$ in a partially inverted $CoAl_2O_4$ [6], whereas in the magnetically diluted system $Co_{1-x}Zn_xAl_2O_4$, the transition occurs at $x_c = 0.06$ [8]. The higher sensitivity of the magnetic ground state with respect to these chemical disorders is due to the magnetic state of $CoAl_2O_4$, which is expected to be located in the vicinity of $J_2/J_1 = 1/8$ where the NSS transition occurs [2], as shown schematically in Fig. 1(b). At the phase boundary, the facts suggest that the transition

*naka.takashi@nims.go.jp

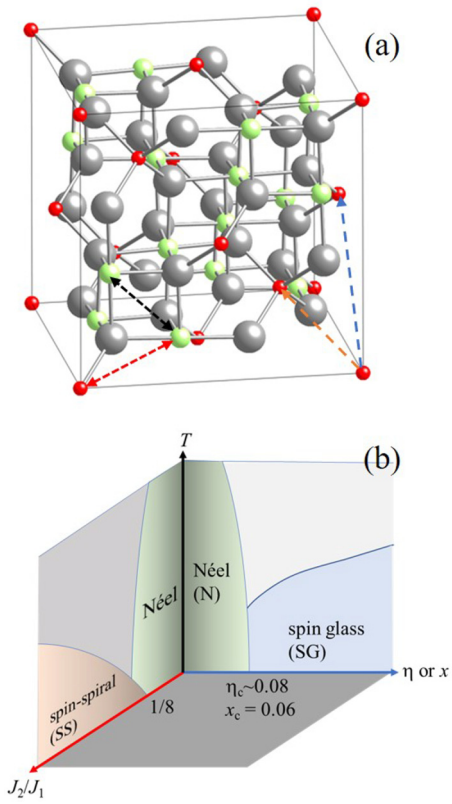

FIG. 1. (a) Spinel structure. Red, yellow, and gray spheres represent the tetrahedral, octahedral cation, and oxygen sites, respectively. Orange and blue dashed lines are connected between nearest and next-nearest neighbor *A*-*A* pairs. Red and black dashed lines represent nearest neighbor *A*-*B* and *B*-*B* pairs, respectively. (b) Schematic phase diagrams of the AB_2O_4 magnet projected into the $\eta(x)$-T [6,8] and (J_2/J_1)-T [2] planes.

temperature is drastically reduced, and concomitantly, the magnetic stiffness constant κ becomes zero; the magnetically ordered states are destabilized at $J_2/J_1 = 1/8$. In other words, a "classical" spin liquid is realized at low temperatures in the vicinity of $J_2/J_1 = 1/8$. The exchange stiffness constant κ is related specifically to the energy cost of magnetically ordered spins when the alignment of neighboring spins coupled with an exchange interaction is distorted infinitesimally from that of the ground state. Experimentally, the magnetic ground state has been proposed to be a spin-glass [6,11], spin-liquid [6,12], unconventionally magnetically ordered [13,14], and antiferromagnetic [15,16] state.

Recent neutron diffraction measurements by MacDougall *et al.* [17] have revealed that (i) an intense Lorentzian scattering component observed in single crystals with $\eta = 0.02 \pm 0.04$ remains even well below the freezing temperature $T^* = 6.5 \pm 1$ K, (ii) an anisotropic Lorentzian-squared character is also established below T^*, and (iii) the observed antiferromagnetic spin wave excitation is consistent with that of antiferromagnetism with a J_2/J_1 value of 0.110 ± 0.003, which is close to the NSS boundary $J_2/J_1 = 0.125$, but falls in the Néel ordered region [Fig. 1(b)], where a first-order phase transition is theoretically expected to occur [2]. A similar value of $J_2/J_1 = 0.109 \pm 0.002$ has been reported by Zaharko *et al.* using a single-crystal specimen with $\eta = 0.05$ [14,18]. Based on these observations, MacDougall *et al.* [17] have hypothesized that there is a peculiar magnetic feature below T^*; that is, the antiferromagnetic domain wall motion is kinetically inhibited, and the long-range antiferromagnetic correlation is therefore blocked. The incomplete magnetic order (the suppression of antiferromagnetic long-range order) found also by Zaharko *et al.* [14,18] immediately suggests that a frozen and fragmented AFM structure is formed. Indeed, the discrepancy between magnetic susceptibilities measured after ZFC (zero field cooling) and FC (field cooling) [6,8,18] and the emergence of the thermoremanent magnetization (TRM) [8] observed in $CoAl_2O_4$ are indicative of small-volume (finite-size) effects and glassy natures. In addition to these phenomena, a relaxation of TRM, a smear-out of a phase transition, and exchange bias are also indicative of nanomagnets [19] and spin glass [20].

The magnetic states of previously examined $CoAl_2O_4$ samples have been located near both the NSS and NSG boundaries [8,15]. This condition seems to be the underlying cause of their controversial behavior with respect to magnetism, and it may account, in particular, for the magnetic ground state and the incomplete magnetic ordering of the *A*-site spinel $CoAl_2O_4$. For $CoGa_2O_4$, in contrast to the case of $CoAl_2O_4$, we might expect that the magnetic states would not be near both boundaries because the degree of chemical disorder is quite sufficient to diminish the effect of magnetic frustration discussed theoretically in Ref. [2] and far from the NSG boundary of $\eta_c \sim 0.08$ [7]. Both the Co and Ga ions are distributed randomly to the *A* and *B* sites. Actually, the inversion parameters determined by powder neutron [21] and single-crystal x-ray [22] diffraction are 0.60 and 0.575(4), respectively. These values of η are comparable with the value of 0.63 obtained by Melot *et al.* for a powder sample [7]. The magnetic ground state of $CoGa_2O_4$ has been postulated to be a spin-glass state below $T \sim 10$ K because the dc-magnetic susceptibility curve shows splitting between field-cooled and zero-field cooled measurements [7,21], and ac susceptibility shows a cusp at $T_f \sim 10$ K [21]. The freezing temperature, T_f, increases with increasing frequency [23]. These spin glass type behaviors are consistent with the fact that neutron diffraction does not show any magnetic reflections at $T = 1.5$ K [21].

In this paper, we report that comprehensive structural and magnetic investigations in the ternary spinel oxide $CoGa_2O_4$ reveal that the inversion parameter is close to that of a random spinel $\eta = 3/2$ and that the cluster spin-glass state is realized below the spin-glass transition at $T_{SG} = 8.2$ K. Remarkably, TRM is observed in $CoGa_2O_4$, and it decays nonexponentially below T_{SG} as a function of time. We demonstrated successfully that a generalized relaxation function based on the stochastic theory of dielectric relaxation derived by Weron [24] was reproduced experimentally in the TRM relaxation. Interestingly, for the insulating spin-glass $CoGa_2O_4$, the parameter q extracted from the TRM relaxation seemed to show a temperature dependence closely resembling that obtained by neutron spin echo measurements [25] in canonical (metallic) spin-glass systems. The parameter q has been characterized as a nonextensive entropy parameter and was originally introduced in a generalization of Boltzmann-Gibbs entropy by

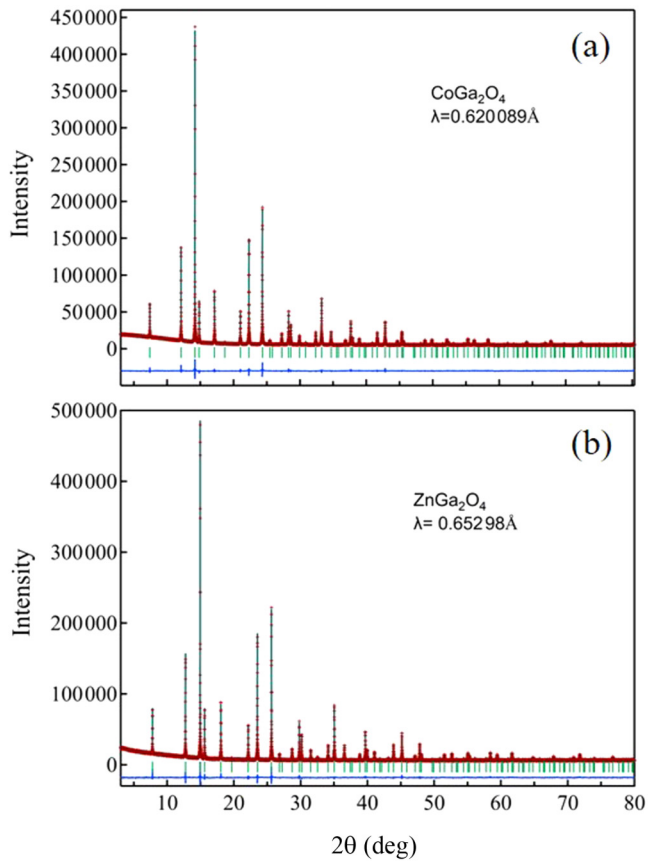

FIG. 2. X-ray diffraction profiles for (a) $CoGa_2O_4$ and (b) $ZnGa_2O_4$. Note that the x-ray wavelengths used for $CoGa_2O_4$ and $ZnGa_2O_4$ are slightly different. The vertical green lines show positions of the Bragg reflections. The difference between observed and calculated intensities is plotted as the lower blue trace.

Tsallis [26,27]. In this study, q was specifically a measure of the collective and hierarchical nature of relaxation phenomena in spin-glass systems [28]. Moreover, the relaxation time $\tau(T)$ obtained from the frequency dependence of the freezing temperature and the TRM decay curve suggested the existence of a crossover in the relaxation process at $T \sim T_{SG}$ from a high-temperature, Vogel-Fulcher type to a low-temperature, quantum mechanical relaxation process. These findings might facilitate further investigation and give insight into the characteristics of the frustrated A-site antiferromagnets, such as $CoAl_2O_4$, the magnetic ground state of which has not yet been revealed.

II. EXPERIMENT

A solid-solid reaction method was used to synthesize $CoGa_2O_4$ and $ZnGa_2O_4$ polycrystalline samples with the proper amounts of CoO (4N), ZnO(4N), and Ga_2O_3 (4N). The mixed powder was calcinated at 1300 °C in ordinary air for 24 h and cooled to room temperature at a rate of 42.5 °C/h. We performed powder x-ray diffraction measurements using a synchrotron x-ray source and made crystal structure refinements with Rietveld analysis software, RIETAN-PF [29]. Powder x-ray diffraction measurements using synchrotron radiation ($\lambda = 0.620\,089$ Å for $CoGa_2O_4$ and 0.652 96 Å for $ZnGa_2O_4$) were conducted on the BL15XU beam line at SPring-8 (Harima, Japan) [30]. The dc and ac magnetizations and specific heat at ambient pressure were measured using a magnetic properties measurement system (MPMS-XL, Quantum Design) and a physical properties measurement system (PPMS Dynacool, Quantum Design), respectively. The error in phase for ac susceptibility was corrected by that measured for a paramagnetic reference material Dy_2O_3. The temperature dependence and relaxation of TRM were measured after field cooling with an excitation dc field of $H_{FC} = 100$ Oe applied at $T = 70$ K. After the measurement temperature $T = T_m$ had been reached, the sample was held at that temperature for $t_m = 100 - 300$ s. The magnetic field was then immediately reduced to zero. Fourier transform infrared (FT IR) spectroscopy was carried out using a conventional spectrometer (FT/IR-6200; JASCO) with KBr pellets.

III. RESULTS

A. X-ray diffraction

Figures 2(a) and 2(b) show x-ray diffraction profiles for $CoGa_2O_4$ and $ZnGa_2O_4$, respectively. Each sample can be assigned to have a cubic spinel structure (space group: Fd-$3m$) with a cationic configuration disorder quantified by the inversion parameter, $\eta = 0.664(8)$ for $CoGa_2O_4$. Because the difference of atomic form factors for Zn and Ga is too small to determine η reasonably by Rietveld refinement, we assumed that the degree of inversion was zero for $ZnGa_2O_4$. The crystallographic parameters and reliable parameters refined by the Rietveld method are listed in Table I. The parameters obtained for $CoGa_2O_4$ in this work are in good agreement with previously reported values [7,21,22].

B. Dc susceptibility

Figure 3(a) shows the temperature dependence of magnetic susceptibility $\chi(T)$ after zero ZFC and FC at $H_{FC} = 100$ Oe. The cusp exhibited by $\chi(T)$ after ZFC at $T = 8.5(5)$ K

TABLE I. Crystallographic parameters and reliability factors obtained by Rietveld refinement for $CoGa_2O_4$ and $ZnGa_2O_4$.

Sample	a (Å)	u	g_A (Co/Zn)[a]	g_A (Ga)	g_B (Co/Zn)[a]	g_B(Ga)[a]	R_{wp}	S
$CoGa_2O_4$	8.32654(1)	0.25844(11)	0.336(8)	0.664(8)	0.332(4)	0.668(4)	4.04	3.56
$CoGa_2O_4$[b]	8.325	0.2582	0.38	0.62	0.31	0.69	–	–
$ZnGa_2O_4$	8.33361(2)	0.26265(14)	1.0	0	0	1.0	5.16	4.85

[a]Constraints: $g_A(\text{Co/Zn}) + g_A(\text{Ga}) = 1$, $2g_B(\text{Co/Zn}) = 1 - g_A(\text{Co/Zn})$, $0.5g_A(\text{Ga}) + g_B(\text{Ga}) = 1$ for $CoGa_2O_4$.
[b]Melot *et al.* [7]. Assumed to be g_A (Zn) = 1.0 and g_B (Ga) = 1.0 for $ZnGa_2O_4$.

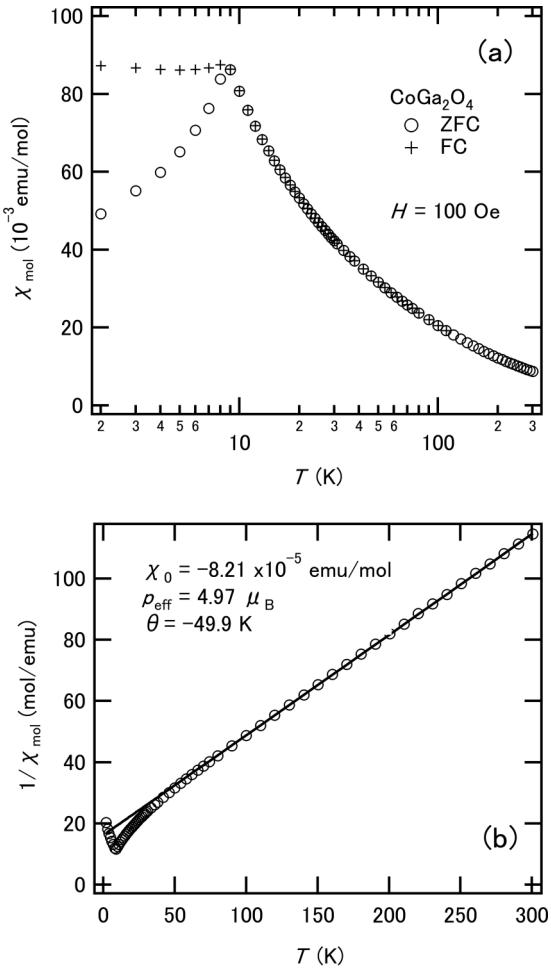

FIG. 3. Temperature dependence of (a) magnetic susceptibility χ_{mol} and (b) reciprocal susceptibility $1/\chi_{mol}$ for $CoGa_2O_4$.

signals a spin-glass transition. As shown in Fig. 3(b), $\chi(T)$ obeys a modified Curie-Weiss law, $\chi(T) = \chi_0 + C/(T-\theta)$, where χ_0, C, and θ are the temperature-independent susceptibility, Curie constant, and Weiss temperature, respectively. The constant susceptibility $\chi_0 = -8.21(1)\times10^{-5}$ emu/mol (Langevin diamagnetic susceptibility) obtained by measuring $\chi(T)$ for $ZnGa_2O_4$ was evaluated as the constant susceptibility for $CoGa_2O_4$. The parameters estimated by the least squares method are $C = 3.08(0)$ and $\theta = -49.9(3)$ K. The effective moment $p_{eff} = 4.97(0)\,\mu_B$, which is calculated from the value of C, was close to reported values [7,31] but rather larger than $4.51\,\mu_B$ for $CoAl_2O_4$ [8]. The observation that p_{eff} was larger for $CoGa_2O_4$ than for $CoAl_2O_4$, which has a smaller inversion with $\eta = 0.055$ [8], might have resulted from the significant occupation of the B site ($\eta = 0.66$) by Co^{2+}. The value of p_{eff} was estimated with the simple equation, $p_{eff}^2 = (1-\eta)p_{eff}^2(A) + \eta p_{eff}^2(B)$, where $p_{eff}(A)$ and $p_{eff}(B)$ are the effective moments of the Co^{2+} ions at the A and B sites, respectively. The value of $p_{eff}(B)$, $5.22\,\mu_B$, was significantly larger than that of $p_{eff}(A)$, $4.47\,\mu_B$, and the value of $g[S(S+1)]^{0.5} = 3.87$ for $S = 3/2$ and $g = 2$. If the spin-orbit coupling is negligibly small compared with the octahedral crystal field energy, the $3d$ electronic state of Co^{2+} is split into doubly degenerate $d\gamma$ and triply degenerate $d\varepsilon$ states by the tetrahedral or octahedral ligand fields, but the $d\gamma$ ($d\varepsilon$) state lies below the $d\varepsilon$ ($d\gamma$) state for Co^{2+} ions that occupy A sites (B sites). The electronic configurations of Co^{2+} in the A site and B site can be represented with $(d\gamma)^4(d\varepsilon)^3$ and $(d\varepsilon)^5(d\gamma)^2$, respectively. The latter therefore has an orbital degree of freedom, that is, $2\upsilon + 1 = 3$, where $\upsilon = 1$ is a pseudo orbital moment for the $(d\varepsilon)^5(d\gamma)^2$ configuration. The former has no orbital degree of freedom because $\upsilon = 0$ for the $(d\gamma)^4(d\varepsilon)^3$ configuration. As mentioned below, however, the spin and orbital (configurational) degrees of freedom involved with the inverted Co^{2+} ion, which was primarily associated with $CoGa_2O_4$, seemed to be reduced by spin-orbit coupling.

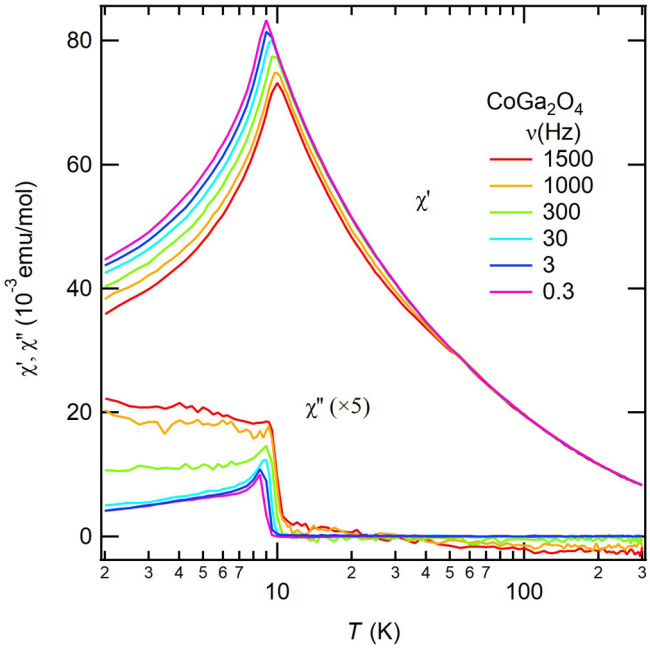

FIG. 4. Real (χ') and imaginary (χ'') components of the ac susceptibility as a function of temperature at various frequencies.

C. Ac susceptibility

The spin-glass state can be confirmed by the dynamical response of the frequency dependence of ac susceptibility within the frequency range $0.3 \leqslant \nu \leqslant 1500$ Hz in the vicinity of the transition. Figure 4 shows the real (χ') and imaginary (χ'') components of the ac susceptibility $\chi(\nu)$ as a function of temperature at various frequencies. $\chi'(T)$ exhibits a cusp at the freezing temperature T_f, which decreases with increasing frequency ν. The maximum value of χ'(at $T = T_f$) decreases with increasing ν. These frequency-dependent characteristics are typically observed in spin-glass systems. Note that in addition to the spin-glass behavior around $T = 9$ K, a weak frequency dependence in $\chi'(T)$ is observable at high temperatures below 50 K. The relaxation time $\tau_{ac} = \nu^{-1}$, the mean time for spin flipping, shows a divergence due to the critical slowing down at the spin-glass transition temperature $T_{SG} = 8.2$ K (see Appendix A). The temperature dependence of τ_{ac} deviates remarkably from the Arrhenius law $\tau_{ac}(T) = \tau_0 \exp(E_a/k_B T)$ (Fig. 5). It is generally recognized that in a spin-glass system, magnetic clusters form that consist of strongly interacting spins blocked in random directions

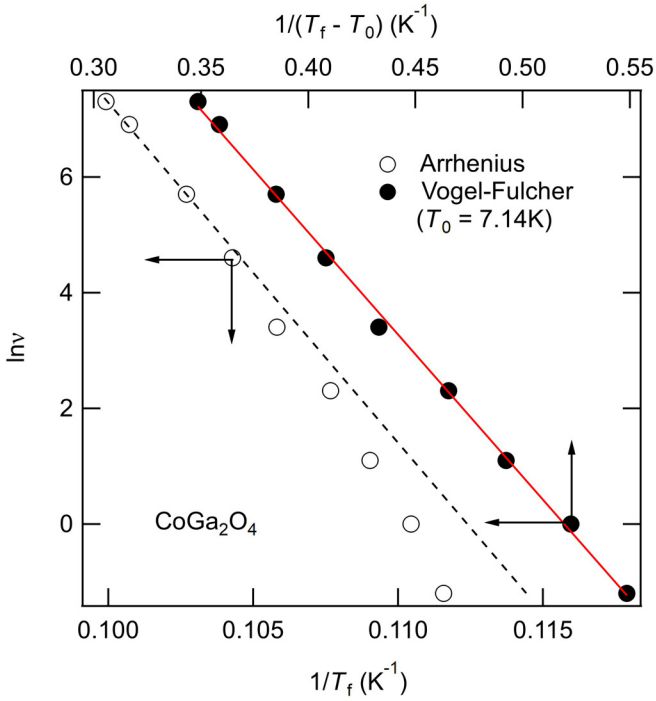

FIG. 5. Semilogarithmic plot of frequency ν versus $1/T_f$ (Arrhenius plot) and $1/(T_f - T_0)$ (Vogel-Fulcher plot). Dashed and solid lines represent least squares fitting curves of the Arrhenius function at high frequencies and the Vogel-Fulcher function, respectively.

whose size and correlation length ξ grow with decreasing temperature. Consequently, $\tau(T)$ tends to diverge at low temperatures. The deviation from the Arrhenius law suggests that a temperature-dependent activation energy can be employed. The strong temperature dependence of τ evidenced in $CoGa_2O_4$ can be described by an empirical equation, the so-called Vogel-Fulcher law,

$$\tau_{ac}(T) = \tau_0 \exp\left[\frac{E_a}{k_B(T_f - T_0)}\right], \quad (1)$$

where τ_0, k_B, and T_0 are the characteristic time for spin flipping, the Boltzmann constant, and the material-dependent characteristic temperature (denoted as the Vogel-Fulcher temperature), respectively (see Fig. 5). Based on the derivation of the quantities in Eq. (1) in the intermetallic spin-glass compound $PrRhSn_3$ [32], one can derive $\tau_0 = 2.86 \times 10^{-10}$ s, $E_a/k_B = 42.3(6)$ K, and $T_0 = 7.14(3)$ K for $CoGa_2O_4$. The value of τ_0 is considerably larger than the values of typical canonical spin-glass systems (e.g., $\tau_0 \sim 10^{-12}$ s for single spin flipping process). The slow dynamics observed in $CoGa_2O_4$ suggests that strongly interacting clusters are established in the glass state. The experimentally obtained parameters of $\Delta T_f/T_f \Delta \log \nu = 0.028$ (comparable to that of the cluster-glass system $PrRhSn_3$), $(T_f - T_0)/T_f = 0.22$ (comparable to that of a short-range interaction spin-glass system), and $E_a/k_B T_f = 5.9$ at $\nu = 3$ Hz (comparable to those of $Eu_{0.4}Sr_{0.6}S$ and Mn aluminosilicate) lie in the range of the empirical values for insulating, short-range interaction spin-glass systems, and most probably cluster glass [33]. The implication is therefore that the random spinel $CoGa_2O_4$ undergoes a cluster-glass transition at $T_{SG} = 8.2$ K.

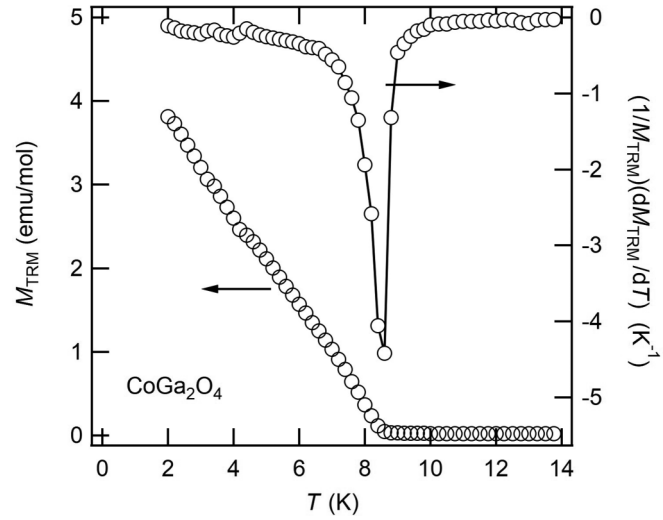

FIG. 6. M_{TRM} and $(1/M_{TRM})(dM_{TRM}/dT)$ as a function of temperature.

D. Thermoremanent magnetization

Generally, thermoremanent magnetization (TRM) is associated with spin glasses or superparamagnetism [34–36]. Since the discovery of spin-glass TRM, it has been used as a probe of the field-quenched state in spin glasses [35,36] and of aging (i.e., memory and rejuvenation) effects realized in spin and also cluster glasses [37,38]. Here we focus on both its magnetic relaxation and critical behavior in the vicinity of and below T_{SG}. In $CoGa_2O_4$ and also in the isostructural $CoAl_2O_4$, the spin-glass state is induced by the chemical disorder that accompanies the enhancement of TRM [8]. Actually, the value of TRM, M_{TRM}, increases monotonically with increasing η [39] and is enhanced anomalously at the magnetic phase boundary in a diluted system [8]. The relaxation and relaxation component ratio of TRM for $CoGa_2O_4$ can signal features of magnetic properties, as shown below. $M_{TRM}(T)$ develops rapidly below T_{SG}, but it is clearly apparent even slightly above T_{SG} under our experimental conditions, whereas the derivative of TRM with respect to temperature shows a steplike enhancement at $T = 8.2$ K (not shown). The logarithmic derivative, $d\ln M_{TRM}/dT [\approx (1/M_{TRM})(dM_{TRM}/dT)]$, shows a more definitive peak at $T = 8.5$ K, a temperature slightly higher than T_{SG} (Fig. 6). Similarly, the relaxation ratio, defined as $\Delta M_{TRM}/M_{TRM} = [M_{TRM}(t_f) - M_{TRM}(t_i)]/M_{TRM}(t_i)$, which is extracted from the isothermal decay curve at various temperatures [Fig. 7(a)], exhibited a sharp peak at $T = 8.2$ K, which corresponds to the spin-glass transition temperature $T_{SG} = 8.2$ K obtained above [Fig. 7(b)]. Here t_i and t_f are the initial and final points in the decay curves, respectively. Note that one can derive $\Delta M_{TRM}/M_{TRM} = -\Delta t/\tau$ if one assumes a Debye-type relaxation $M_{TRM}(t) = M_{TRM}(0)\exp(-t/\tau_D)$, where $M_{TRM}(0)$ and τ_D are the TRM value at $t = 0$ and the relaxation time, respectively, and $\Delta t = t_f - t_i$. Below T_{SG}, the relaxation rate decays rapidly with decreasing temperature, and its temperature variation can be fitted by an Arrhenius function with a constant term, $\Delta M_{TRM}/M_{TRM} \sim a_0 + a_1 \exp(-E_{Arr}/k_B T)$, where a_0 and a_1 are temperature-independent constants, and E_{TRM} is an activation energy for the TRM relaxation [Fig. 7(b)].

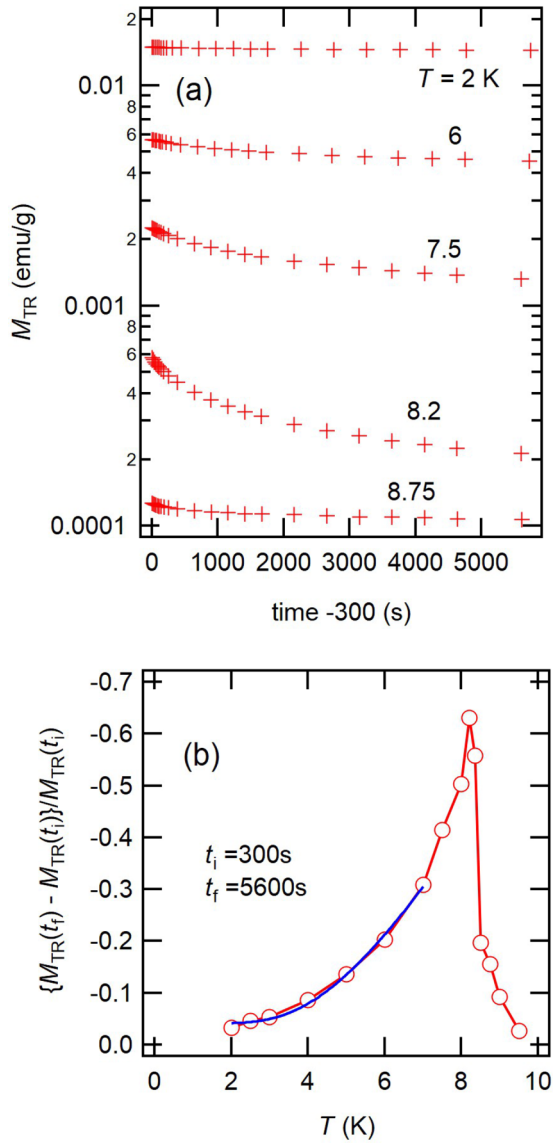

FIG. 7. (a) Decay profiles and (b) temperature dependence of the relaxation rate $[M_{\mathrm{TRM}}(t_{\mathrm{f}}) - M_{\mathrm{TRM}}(t_{\mathrm{i}})]/M_{\mathrm{TRM}}(t_{\mathrm{i}})$ of thermoremanent magnetization M_{TRM}. Red solid line is a guide to aid visualization. Blue solid line represents a fitting curve to an Arrhenius function (see text).

We extracted the quantities, $a_0 = -0.041(5)$, $a_1 = -3.5(7)$, and $E_{\mathrm{Arr}}/k_{\mathrm{B}} = 18(2)$ K by a least squares fitting to the Arrhenius function. As shown below, the value of $E_{\mathrm{TRM}}/k_{\mathrm{B}}$ was consistent with the temperature when the specific heat is a maximum. Consequently, we can roughly estimate $\tau_{\mathrm{D}}(T)$ at $T = 2$ K and T_{SG} to be $\sim 10^6$ and 10^4 s, respectively. These times are one order of magnitude larger than the values obtained directly from the isothermal decay curves of M_{TRM} fitted by other decay functions (see Appendix B). Instead, the $M_{\mathrm{TRM}}(t)$ curve is reproduced by the so-called stretched exponential and other functional forms, as mentioned below.

Figures 8(a) and 8(b) show isothermal curves of $M_{\mathrm{TRM}}(t)$ at $T = 3$ ($<T_{\mathrm{SG}}$) and 8.5 K ($>T_{\mathrm{SG}}$), respectively, as a function of time after the excitation field ($H_{\mathrm{FC}} = 100$ Oe) had been turned off. In advance, the sample was field cooled with

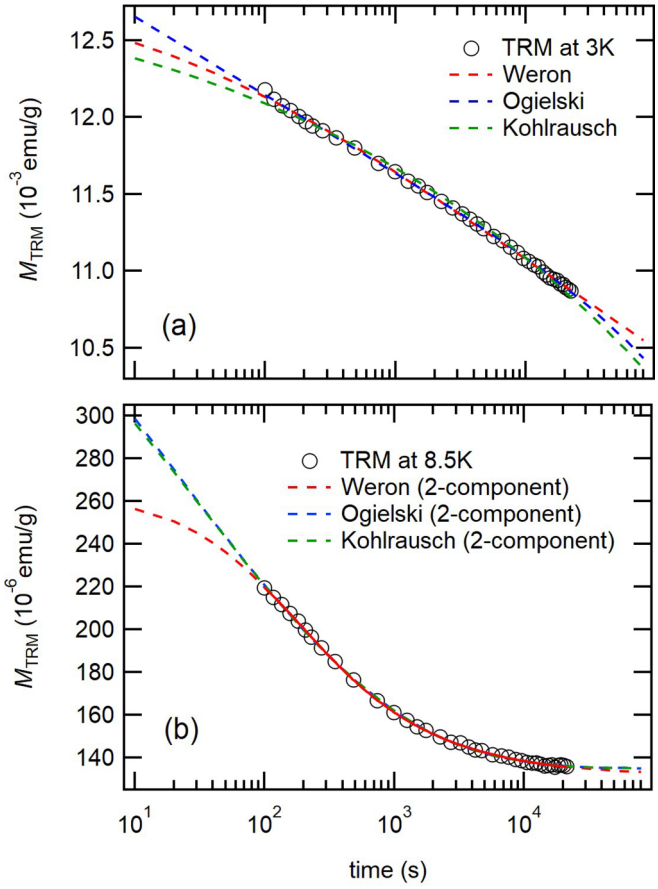

FIG. 8. Isothermal decays of M_{TRM} measured at (a) $T = 2$ K and (b) 8.5 K. The red, blue, and green dashed lines represent curves obtained by least squares fitting of the Weron, Ogielski, and Kohlrausch relaxation functions, respectively.

$H_{\mathrm{FC}} = 100$ Oe from 70 K to the measurement temperature T. Before measuring $M_{\mathrm{TRM}}(t)$ at the measurement temperature, the magnetic field $H_{\mathrm{FC}} = 100$ Oe was kept for a waiting time $t_{\mathrm{w}} = 300$ s. It is apparent that the profiles of $M_{\mathrm{TRM}}(t)$ change qualitatively at $T \sim T_{\mathrm{SG}}$ [Figs. 8(a) and 8(b)]. Below T_{SG}, the variation of M_{TRM} with time for $CoGa_2O_4$ follows fairly typical relaxation functions: a stretched exponential (Kohlrausch), or the Ogielski and Weron functions (see Appendix B) with reasonable parameters. Figure 8(a) shows the isothermal decay of M_{TRM} at 3 K with least squares fits for the Weron, Ogielski, and Kohlrausch functions displayed by red, blue, and green dashed lines, respectively. The $M_{\mathrm{TRM}}(t)$ curve is reproduced fairly well by the Weron and Ogielski functions but not as well by the Kohlrausch function. As demonstrated in Appendix C, the t_{w}-dependent behavior, which is one of the aging effects often apparent in TRM decay for spin and cluster glasses [36,39], can be neglected for $CoGa_2O_4$ to facilitate extraction of the relaxation parameters for the relaxation functions from the fitted $M_{\mathrm{TRM}}(t)$ curve. Above and in the vicinity of the spin-glass transition, a time-independent component term must be added to these functions to reproduce the $M_{\mathrm{TRM}}(t)$ curve:

$$M_{\mathrm{TRM}} = p_0 + p_1\phi(t), \tag{2}$$

where p_0 and p_1 are time-independent constants (magnetization components), and $\phi(t)$ is the relaxation function mentioned above [Fig. 8(b)]. Note that the residual field H_{res} in the magnetometer, which was estimated to be a few tenths of an oersted, can make an extrinsic contribution to the value of p_0, which is estimated to be $M_{res} = \chi(T \sim T_{SG})H_{res} \sim 1 \times 10^{-4}$ emu/g ($\sim 3 \times 10^{-2}$ emu/mol). This value is comparable to the value of p_0 observed at 9 K.

Here we employ the Weron relaxation function (Appendix B) with a constant term p_0 to reproduce the isothermal decay curves of M_{TRM}. In the vicinity of the spin-glass transition at $T = T_{SG}$, parameters obtained by employing both the one-component ($p_0 = 0$) and two-component ($p_0 \neq 0$) models are compared in Figs. 9(a)–9(c) and 10. The total moment $p_{tot} = p_0 + p_1$ increases rapidly in the vicinity of the spin-glass transition at $T_{SG} = 8.2$ K. The temperature variation of p_{tot} is rather well described by $p_{tot}(T) = p^0_{tot}(1-T/T_{SG})^{\alpha}$ at $T < T_{SG}$ with $p^0_{tot} = 4.7(1)$ emu/mol and $\alpha = 0.77(5)$. Here, p^0_{tot} is the TRM at $T = 0$. The exponent β stays at $\sim$0.5 below the transition, but it increases rapidly to $\sim$1.0 at temperatures close to T_{SG} [Fig. 9(b)]. The coefficient k decreases with increasing temperature and approaches zero at high temperatures [Fig. 9(c)]. Note that in the limit of $k = 0$ and $\beta = 1.0$, the decay function asymptotically approaches a Debye function $p_1 \exp(-t/\tau)$. The implication is that TRM relaxation above the spin-glass transition can be associated with a single spin flip with a weak magnetic correlation between spins. Moreover, the relaxation time τ increases with decreasing temperature and apparently follows an Arrhenius law with an activation energy $E_a \sim 100$ K at $T \sim T_{SG}$ and $E_a < 10$ K at $T \ll T_{SG}$. As shown in Fig. 10, at $T \sim T_{SG}$, the $\tau_W(T)$ and $\tau_D(T)$ curves approach the extrapolated curve of $\tau_{ac}(T)$ in accord with the Vogel-Fulcher law (Fig. 5). In contrast, above T_{SG} the tendency of $\tau_{ac}(T)$ differs considerably. The discrepancy between τ_{ac} and τ_W is reconsidered below.

Here, we propose that the relaxation of the TRM may occur through either of two mechanisms: (1) the Vogel-Fulcher (VF) law and (2) an Arrhenius law with a small E_a, or a temperature-independent relaxation mechanism, such as a quantum mechanical process, i.e., tunneling through a potential barrier:

$$\frac{1}{\tau_{tot}} = \frac{1}{\tau_{VF}} + \frac{1}{\tau_{Arr}} \tag{3}$$

(see Fig. 10). As shown above, it is plausible that τ_{VF} diverges exponentially at $T_0 = 7.14$ K. At $T \ll T_{SG}$ the temperature dependence of τ_{TRM} might be suppressed, and τ_{tot} may become nearly constant because of the presence of the second term in Eq. (3). It is generally established that the relaxation time τ scales with the number of relaxing units N or effective volume v of magnetic clusters responsible for magnetic relaxation according to a generalized expression such as $\tau = v^{1/\gamma}$ with $0 \leqslant \gamma \leqslant 1$ [28]. Consequently, the cluster size might be saturated at $T \ll T_{SG}$ in $CoGa_2O_4$, but it might not actually diverge anymore at $T = T_0$. In contrast, it is apparent in glass-forming liquids that the temperature variation of viscosity follows the VF law; i.e., viscosity diverges at T_0 below the glass transition temperature [40].

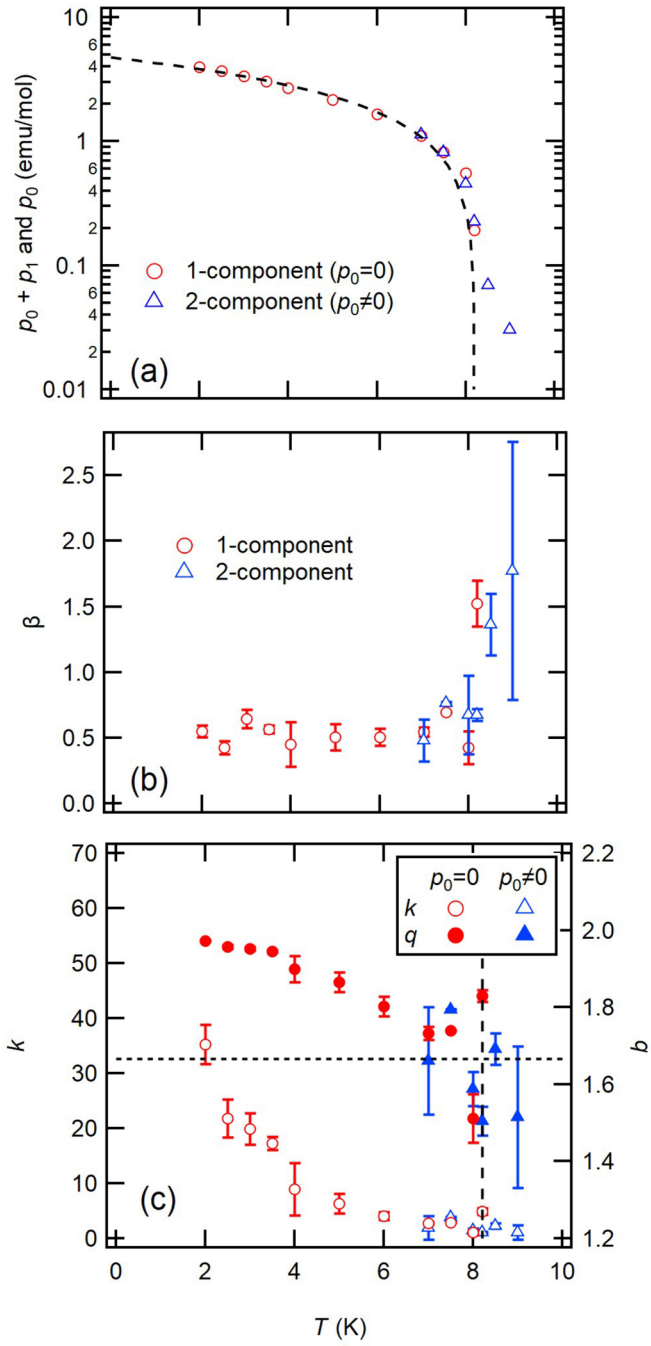

FIG. 9. Temperature dependences of (a) $p_{tot} = p_0 + p_1$, (b) β, and (c) k and q. Dashed curve in (a) represents a numerically fitted curve that corresponds to $p_{tot}(T) = p^0_{tot}(1-T/T_{SG})^{\alpha}$ with $p^0_{tot} = 4.4$ emu/mol and $\alpha = 0.77$. Vertical and horizontal dashed lines in (c) indicate $q = 5/3$ and $T = T_{SG}$, respectively.

Figure 9(c) shows the temperature dependence of k, which is called the interaction parameter. k is related with the waiting time and the collective nature of the interaction and associated with the nonextensivity parameter q via the simple equation $q = (2k+1)/(k+1)$ [28] (see Appendix B). The value of q varies in the range $1 < q < 2$ when $k > 0$. Theoretical findings reveal that the extensive-nonextensive critical phenomenon at $q = 5/3$ is expected to occur in

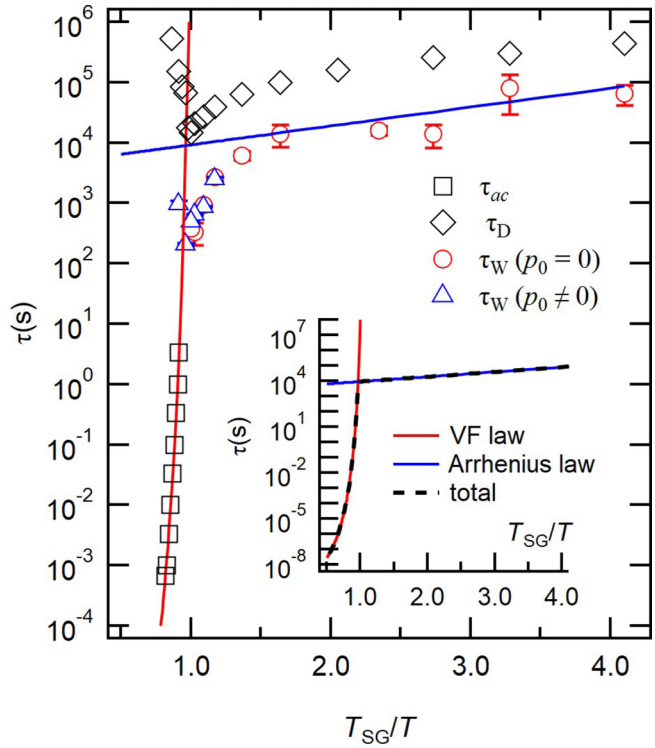

FIG. 10. Relaxation time τ as a function of T_{SG}/T. τ_{ac} is obtained by a least squares fitting ac-$\chi(\nu)$. τ_D and τ_W are obtained by numerical fittings of the decay curve of $M_{TRM}(t)$ with Debye and Weron relaxation functions, respectively. Inset shows τ_{VF}, τ_{Arr}, and τ_{tot} as a function of T_{SG}/T represented by red and blue solid lines and a black dotted line, respectively.

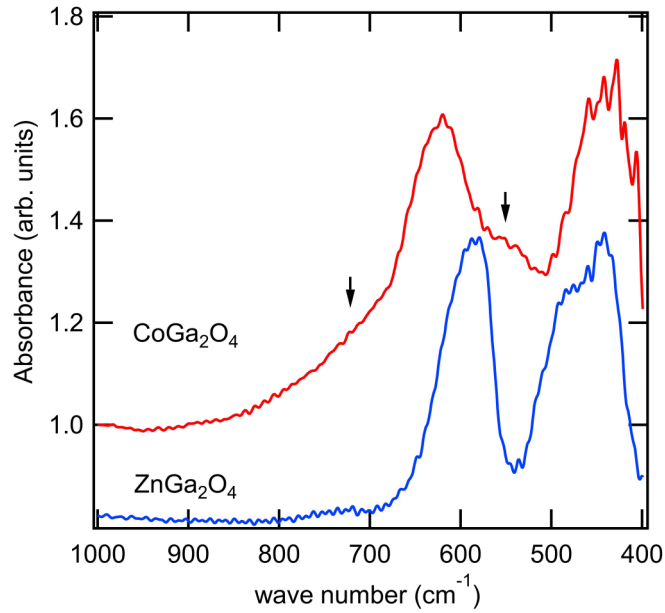

FIG. 11. FT IR spectra for $CoGa_2O_4$ and the isostructural compound $ZnGa_2O_4$. Arrows indicate the broad peak and shoulder observed at 560 and 720 cm^{-1}, respectively.

complex physical systems such as glasses, polymers, and colloids [26]. In various metallic canonical spin-glass systems, measurement of the neutron spin echo has demonstrated that the $q(T)$ curves collapse in a curve with $q \sim 5/3$ at the spin-glass transition $T = T_{SG}$, whereas $q(T)$ asymptotically approaches $q = 2$ at $T = 0$ and reaches $q = 1$ at $T \sim 1.5T_{SG}$ [25]. Surprisingly, the $q(T)$ obtained from the relaxation curves $M_{TRM}(t)$ of $CoGa_2O_4$ follow the $q(T)$ subtracted from the neutron spin echo spectra $S(Q, t)$ in canonical (metallic) spin glasses, where Q is the scattering vector and t is in the range 0.01–10 ns.

E. FT IR spectra

A comparison of the FT IR spectra of $ZnGa_2O_4$ and $CoGa_2O_4$ facilitated detection of the inversion effect on the infrared (IR) spectrum of $CoGa_2O_4$, which is sensitive to structure and the nature of bonding. Figure 11 shows the FT IR spectra for $ZnGa_2O_4$ and $CoGa_2O_4$. The IR spectral peaks assigned theoretically to the T_{1u} mode [41] were observed at the IR frequencies listed in Table II for $ZnGa_2O_4$. For the $ZnGa_2O_4$ synthesized in this study, the strong peaks at 582 and 439 cm^{-1} corresponded well with previously calculated [41] and observed [42] values. Contrary to the case of $ZnGa_2O_4$, a shoulder and a broad peak were observed at 720 and 560 cm^{-1}, respectively, in the spectra of $CoGa_2O_4$ (Fig. 11). Compared with that of $ZnGa_2O_4$, the IR spectrum of $CoGa_2O_4$ shifted as expected toward higher frequencies when the mass difference between Co and Zn was considered. The shift was estimated to be detectable but small, e.g., $(m_{Zn}/m_{Co})_{1/2} = 1.05$. Actually, for the Zn and Co aluminates with $\eta < 0.055$, the shift of the IR peak position was negligibly small [43]. As shown in Fig. 11 and Table II, the IR peak at 620 cm^{-1} of $CoGa_2O_4$ was shifted from the peak at 582 cm^{-1} of $ZnGa_2O_4$ by a factor of 1.07, slightly larger than the 1.05 estimated above, whereas the IR peak at 434 cm^{-1} might have been shifted toward lower frequency. In the largely inverted $CoGa_2O_4$, the additional structures of the IR spectra seemed to be related to the tetrahedrally coordinated Ga^{3+} and the

TABLE II. Calculated and observed FT IR mode frequencies (unit: cm^{-1}) for $ZnGa_2O_4$, $CoGa_2O_4$, and $NiAl_2O_4$.

$ZnGa_2O_4$[a]	$ZnGa_2O_4$	$ZnGa_2O_4$	$CoGa_2O_4$	$NiAl_2O_4$
580	570	582	720^s	810^s
429	420	439	620	715
342	328		560^b	600^b
175	175		434	505
[41]	[42]	This work	This work	[44]

[a]Calculated values. *s*: shoulder. *b*: broad peak.

octahedrally coordinated Co^{2+} ions. Whereas the mass difference between Co and Ga is relatively small, the phonon modes are rather strongly modified by the inversion, at least in the region $550 - 850\,cm^{-1}$. Note that in this study, the IR phonon modes below $400\,cm^{-1}$ of the spinel compounds were not detected because the lower-frequency limit of the spectrometer was $398\,cm^{-1}$. These inversion-induced structures are also apparent in the inverse spinel $NiAl_2O_4$ with $\eta = 1$ (Table II) [44] and the partially inverted $ZnAl_2O_4$ nanoparticles with $\eta = 0.34$ [45]. The spectral intensity of the shoulder at $790\,cm^{-1}$ diminishes with decreasing η in $ZnAl_2O_4$ nanoparticles annealed subsequently at various temperatures up to 1273 K [45,46]. The shoulder has been claimed to be indicative of the presence of the inverted Al^{3+} ion [45,46]. It is plausible that in the IR spectrum of $CoGa_2O_4$, the shoulder at $810\,cm^{-1}$ is accompanied with the IR modes involving a Ga^{3+} ion at the *A* site.

F. Specific heat

The magnetic state in $CoGa_2O_4$ was also characterized by specific heat measurements. The specific heat divided by temperature C_{mol}/T exhibits a broad maximum at $T = 10$ K accompanied by a glass transition at $T_{SG} = 8.2$ K [Fig. 12(a)]. To calculate the magnetic component of the specific heat ΔC_{mol} and magnetic entropy S_{mag} we needed to estimate the lattice contribution of the specific heat $C_{lattice}$ for $CoGa_2O_4$. Theoretical considerations indicate that for $ZnGa_2O_4$ the partial phonon density of states (PDOS) for the heavy Zn and Ga ions is distributed mainly below $360\,cm^{-1}$, whereas for the light oxygen ion the partial PDOS is distributed above $360\,cm^{-1}$ [41]. At low frequency, the PDOS seems to exhibit a Debye-type parabolic frequency dependence that consists mainly of the contributions of Zn and Ga ions. We can apply the Einstein-Debye (ED) model to obtain $C_{lattice}$ for MAl_2O_4 (M = Zn, Co, Fe, Mn) [11] and for $CoAl_2O_4$ [16]. We followed the analytical procedures for aluminate oxides [11] and first made a fit of C_{mol}/T for $ZnGa_2O_4$ to the ED function to obtain the Debye and Einstein temperatures (Table III). The ED function,

$$C = 3Ra_D x_D^{-3}\int_0^{x_D}\frac{x^4 e^x}{(e^x-1)^2}dx + R\sum_{k=1}^{2} a_{E_k}\frac{x_{E_k}^2 e^{x_{E_k}}}{\left(e^{x_{E_k}}-1\right)^2}, \quad (4)$$

consists of two terms and is based on the Debye-Einstein model with the three coefficients determined experimentally, i.e., the Debye temperature Θ_D and Einstein temperatures Θ_{E1} and Θ_{E2}. The lattice degrees of freedom (LDF) for spinel compounds are distributed to one acoustic and two optical modes. Here, $x_i = \Theta_i/T$ ($i = D$, E_1, E_2) are the reduced inverse temperatures, a_i is the number of LDF, and R is the gas constant. The Dulong-Petit rule predicts that in a three-dimensional lattice, the molar specific heat is $3rR$, which is reproduced asymptotically by the ED function at high temperatures ($T \gg \Theta_D$, Θ_{E1}, and Θ_{E2}), where r is the number of atoms per formula unit [47]. The factor $3r = 21$ is the number of LDF in a cubic spinel structure. The temperature variation of C_{mol}/T for $ZnGa_2O_4$ was reproduced using the ED function with the coefficients shown in Table III. Compared with $\Theta_D = 286$ K for $ZnAl_2O_4$ [11], the reduction of Θ_D for $ZnGa_2O_4$ by a factor of 0.85 was in good agreement with the scaling factor of 0.82 derived analytically for a ternary compound [48]. In the ED function employed for the spinel compounds [11], the Einstein modes represented by E_1 and E_2 had 12 and six optical degrees of freedom, respectively, whereas the Debye

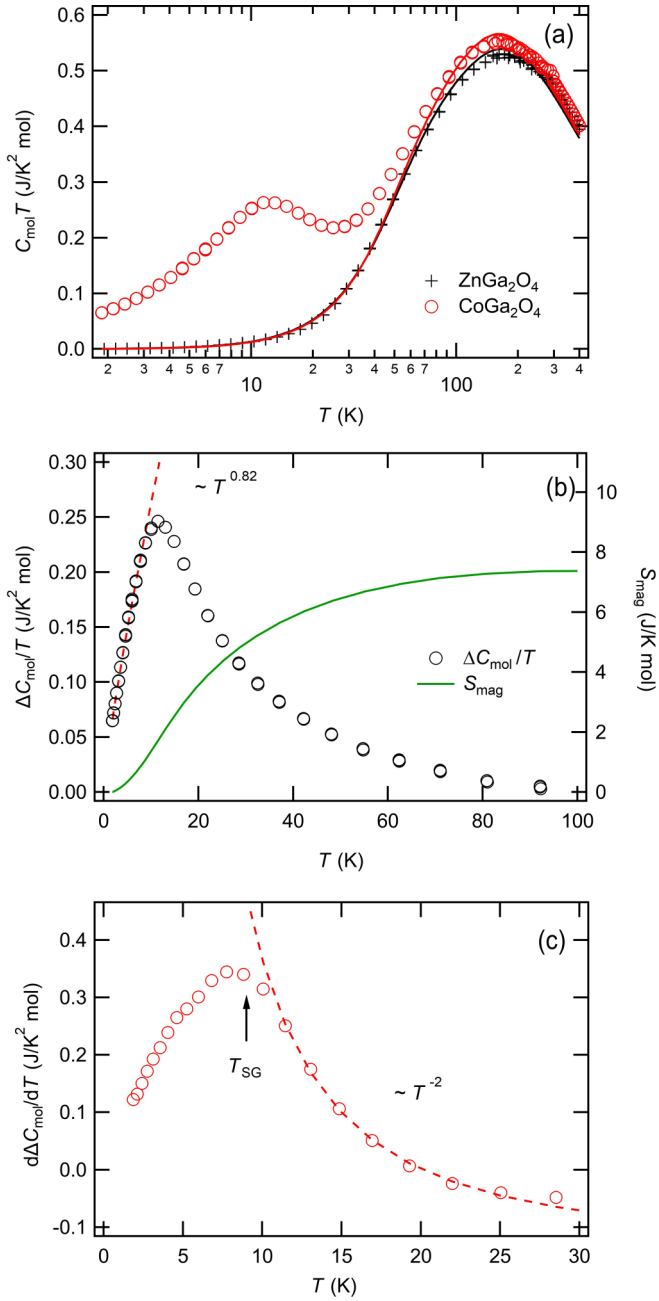

FIG. 12. (a) Temperature variations of C_{mol}/T for $CoGa_2O_4$ and the isostructural compound $ZnGa_2O_4$. Red and black lines represent $C_{lattice}/T$ obtained by least squares fitting to the Einstein-Debye model for $CoGa_2O_4$ and $ZnGa_2O_4$, respectively. (b) Black open circles show the magnetic component $\Delta C_{mol}/T = [C_{mol}(CoGa_2O_4) - C_{lattice}]/T$. The magnetic entropy S_{mag} is also depicted. The dashed line represents a power law with respect to temperature $\Delta C_{mol}/T = 0.054T^{0.82}$. (c) The temperature derivative of ΔC_{mol} as a function of temperature. Arrow indicates the spin-glass transition point T_{SG}. The dashed red line shows T^2 variation above T_{SG}.

TABLE III. Lattice degrees of freedom a_i ($i = D$, E_1, and E_2) employed in Ref. [11] and Debye and Einstein temperatures for $CoGa_2O_4$, $ZnGa_2O_4$, and related spinel compounds.

Mode[a]	D (A)	E_1 (O)	E_2 (O)	
a_i	3	12	6	21 in total
Temperature	Θ_D (K)	Θ_{E1} (K)	Θ_{E2} (K)	Reference
$CoGa_2O_4$	247[b]	634	301	This work
$ZnGa_2O_4$	244	672	310	This work
$CoAl_2O_4$	301	530	886	[11]
$ZnAl_2O_4$	286	543	1244	[11]

[a]A and O in parentheses represent acoustic and optical modes, respectively.
[b]Estimated by a scaling factor of $\Theta_D(CoGa_2O_4)/\Theta_D(ZnGa_2O_4) = 1.013$ [48].

mode had three acoustic degrees of freedom (Table III). It is quite reasonable to deduce for $ZnGa_2O_4$ that the E_1 and E_2 modes were due to oxygen and cation motions, respectively. In other words, the results for Θ_i and a_i ($i = D$, E_1, and E_2) shown in Table III are a coarse graining of the PDOS structure of $ZnGa_2O_4$ [41]. In the case of $ZnAl_2O_4$, the contributions of the motions of both the oxygen and aluminum atoms to the PDOS are primarily above 250 cm^{-1}, whereas the zinc motion contributes below 250 cm^{-1}. Above 700 cm^{-1} and up to more than 1000 cm^{-1}, the PDOS is due to the motion of oxygen [49]. Therefore, the E_1 mode with $a_{E1} = 12$ represents both oxygen and aluminum motions, whereas the E_2 mode with $a_{E2} = 6$ is due to the motion of oxygen at high frequencies above 700 cm^{-1}. The simple ED function can reproduce the temperature variation of the specific heat, and the obtained coefficients are qualitatively consistent with the PDOS structures.

We needed a reasonable estimate of $C_{\rm lattice}$ for $CoGa_2O_4$, because the phonon structure of $CoGa_2O_4$ was modified by the existence of the inverted cations (i.e., the octahedrally coordinated Co^{2+} and the tetrahedrally coordinated Ga^{3+}), as suggested by the comparison of the IR spectra of the aluminates and gallates with various degrees of inversion. It is plausible, therefore, that the specific heat of the nonmagnetic reference material $ZnGa_2O_4$ was not an appropriate $C_{\rm lattice}$ for $CoGa_2O_4$. Assuming that the inversion effect on Θ_D could be neglected for $CoGa_2O_4$, we estimated the value of Θ_D for $CoGa_2O_4$ using the scaling factor $\Theta_D(CoGa_2O_4)/\Theta_D(ZnGa_2O_4) = 1.013$ [48]. We obtained a fairly good fit to the ED function above 90 K [Fig. 12(a)] and obtained the Einstein temperatures (Table III). A small failure in the curve fitting for $C_{\rm mol}/T$ was apparent at $T > 200$ K. It is likely that the A-site substitution from Zn to Co resulted in a considerable shift of the phonon structure related to the motion of oxygen. The magnetic specific heat component $\Delta C_{\rm mol}/T = [C_{\rm mol}(CoGa_2O_4) - C_{\rm lattice}(\Theta_D, \Theta_{E1}, \Theta_{E2})]/T$ and the magnetic entropy

$$S_{\rm mag} = \int_{T_{\rm min}}^{T} \frac{\Delta C_{\rm mol}}{T} dT \qquad (5)$$

were calculated as shown in Fig. 12(b). Here, $T_{\rm min} \sim 1.9$ K was the lowest experimental temperature. $\Delta C_{\rm mol}(T)$ followed the power law $\Delta C_{\rm mol} = \delta T^{1.82}$ with respect to temperature, with $\delta = 54(1)$ mJ $K^{-2.82}$ below $T = 8$ K [Fig. 12(b)], and it exhibited a maximum at $T = 11.5$ K. The exponent 1.82(1) was comparable to and somewhat larger than the typical value of 1.5 observed in spin glasses [50], but it was smaller than the reported values of 2.0 [11,13], 2.1 [18], 2.23 [15], 2.33 [8], and 2.5 [12] for lightly inverted $CoAl_2O_4$ samples. With decreasing temperature, there was a remarkable upturn approximately proportional to T^{-2}, and a kink was apparent in the $d\Delta C_{\rm mol}(T)/dT$ curve [Fig. 12(c)]. Interestingly, the kink position coincided with $T_{\rm SG}$. With a further decrease of temperature, the curve passed over a convex-upward plateau and then decreased monotonically. It is worth noting that $S_{\rm mag}(T)$ seemed to reach a saturation value $S_{\rm mag}$ of 7.5(9) J K^{-1} mol^{-1} at temperatures as high as $T = 100$ K ($\gg T_{\rm SG}$), and $S_{\rm mag}(T)$ was suppressed compared with the experimentally obtained values of 13 at $T = 150$ K [11], 9.47 at $T = 100$ K [15], 10.2 at 60 K [18], 9.9 at 40 K [8], and 8.4 J K^{-1} mol^{-1} at 100 K [16] for $CoAl_2O_4$ as well as for the theoretically expected value of $S_{\rm spin} = R\ln(2S + 1) = 11.52$ J K^{-1} mol^{-1} based on the spin degrees of freedom for $S = 3/2$ of Co^{2+}.

As mentioned above, the magnetic measurement revealed that the effective magnetic moment for the Co^{2+} at the B site was considerably greater than the spin value of $p_{\rm eff} = 3.87\,\mu_B$ for $S = 3/2$. This difference implies that an orbital moment was not completely quenched, and an intermediate ligand field scheme [51] was therefore appropriate for an octahedrally coordinated Co^{2+}; that is, the crystal field and spin-orbit coupling energies seemed to be comparable. The Co^{2+} ($3d^7$) state was described using a fictitious angular moment $\zeta = 1$ that coupled to the spin moment $S = 3/2$ [51]. Spin-orbit coupling resulted in the formation of a $(2\zeta+1)(2S+1)$ manifold of $J' = \zeta + S$ consisting of three states of $J' = 5/2$, $3/2$, and $1/2$. The ground state was the doublet of $J' = 1/2$. The energy separation between the ground and low-lying $J' = 3/2$ states was estimated to be approximately 580 K for the octahedral Co^{2+} ion. This energy difference was a result of spin-orbit coupling λ' ($\boldsymbol{\zeta}\cdot\boldsymbol{S}$), where λ' is an effective spin-orbit parameter. Therefore, the estimated specific heat involved with the excited states seemed to be negligibly small in the temperature range $T < 100$ K. For $CoGa_2O_4$, the magnetic entropies of the tetrahedral and the octahedral Co^{2+} ions were $(1-\eta)R\ln(4)$ and $\eta R\ln(2)$, respectively. The experimental value of $S_{\rm mag} = 7.5$ J K^{-1} mol^{-1} at $T = 100$ K was, within experimental error, equal to $(1-\eta)R\ln(4) + \eta R\ln(2) = 7.70$ J K^{-1} mol^{-1}. For the octahedrally coordinated Co^{2+} ion, the doublet grand state stabilized by the effective spin-orbit coupling was also apparent in the garnet $NaCa_2Co_2V_3O_{12}$, which exhibited an antiferromagnetic transition at $T_N = 6.4$ K [52], as well as the silver delafossite $Ag_3Co_2SbO_6$ with $T_N = 21.2$ K [53].

IV. DISCUSSION AND CONCLUSIONS

We demonstrated by measurements of the dc- and ac-magnetic susceptibilities and TRM that cluster glass is established below the transition at $T_{\rm SG} = 8.2$ K in $CoGa_2O_4$. In addition, the realization that TRM was a macroscopic phenomenon proved that there is a mechanism of magnetic relaxation in the glass state. In the following discussion, we

summarize the results for $CoGa_2O_4$ that were different from or comparable to previously reported characteristics of other spin and cluster glasses.

The cationic configuration in $CoGa_2O_4$ is close to that of a random spinel characterized by a degree of inversion $\eta = 2/3$. The Rietveld refinement revealed that the inversion of our polycrystal sample was 0.664(8). The implication is that both the A-site and B-site occupancies of the magnetic Co^{2+} ion, g_A(Co) and g_B(Co), respectively, were greater than the percolation threshold $x_c^{AB} = 0.227(3)$, but they were smaller than the A-site and B-site thresholds $x_c^A = 0.429(3)$ and $x_c^B = 0.390(3)$ [54], respectively. The Co^{2+} ions with $S = 3/2$ were distributed in both the sites and form macroscopic magnetic clusters if the nearest neighbor super-exchange interactions J_{AB} and J_{BB} are anticipated between spins. These circumstances eliminate the bond frustration expected to exist in the A-site spinel antiferromagnet and also induce the cluster glass state. The octahedrally coordinated Co^{2+} ion is known to display weak Jahn-Teller activity because of the orbital (configurational) degree of freedom. Because in $CoGa_2O_4$ the g_B(Co) is less than x_c^B, it seems theoretically possible that a cooperative Jahn-Teller transition is not realized. In actuality, the crystal structure of $CoGa_2O_4$ is always a cubic spinel.

The relaxation rate $1/\tau_D$ and the temperature derivative of the $M_{\rm TRM}$ are sensitive to the spin-glass transition at $T_{\rm SG}$. They exhibit sharp peaks at $T_{\rm SG}$ [Figs. 6 and 7(b)]. It is worth noting that the frequency-dependent ac susceptibility is observed below $T \sim 50$ K (Fig. 4), which seems to suggest that $CoGa_2O_4$ undergoes a short-range magnetic order. Since the imaginary component $\chi''(T)$ does not show an anomaly at $T \sim 50$ K, it is plausible that an antiferromagnetic cluster embedded in paramagnetic spins is developed at $T \gg T_{\rm SG}$ [55]. This speculation is supported by the discrepancy between the temperature variations of $\tau_{\rm ac}$ and τ_D observed at $T > T_{\rm SG}$, as shown in Fig. 10; that is, a two-component model can be employed for describing the magnetic state of $CoGa_2O_4$. Therefore, more plausibly, an inhomogeneous magnetic phase, e.g., a Griffiths phase emerges below $T = |\theta|$ where θ is the Weiss temperature obtained in the paramagnetic state, as speculated to be realized in $CoAl_{2-x}Co_xO_4$ at $x > 0.9$ [56]. These situations for $CoGa_2O_4$ remind us that in a Co_3O_4 nanoparticle system a spin-glass-like transition occurs at $T = 10$ K, while an antiferromagnetic transition is indicated at $T = 32$ K close to the Néel point for a bulk sample [57]. Below the Néel point a ferromagnetic component arises and develops with decreasing temperature. Interparticle magnetic interactions realized in the antiferromagnetic nanocrystals randomly oriented bring about the spin-glass-like transition.

In $CoGa_2O_4$ the saturation tendency of the relaxation time (i.e., cluster volume) observed at low temperatures $T < T_{\rm SG}$ reflects the fact that in the A-site frustrated antiferromagnet $CoAl_2O_4$, the magnetic correlation length remains on the order of nanometers at well below the Néel temperature [17,18]. The absence or suppression of long-range ordering in $CoGa_2O_4$ might be due to the large degree of inversion. Concomitantly, the Co^{2+} ion occupying the octahedral B site might have brought about the formation of the magnetic cluster. In fact, $M_{\rm TRM}$ is enhanced as η increases with increasing x in $CoAl_{2-x}Ga_xO_4$ [39]. On the other hand, the suppression of long-range magnetic ordering in $CoAl_2O_4$ seems to result from the proximities to the NSS boundary of $J_2/J_1 = 1/8$ and the NSG boundary of $\eta_c = 0.08$ [Fig. 1(b)]. While relaxation time $\tau(T)$ reflects the inherent characteristics in $CoGa_2O_4$, apparent magnetic behaviors might be quite universal as those expected to be observed in a spin or cluster glass as follows. At $T = T_{\rm SG}$ the nonextensive parameter is $q \sim 5/3$ for $CoGa_2O_4$; where the extensive-nonextensive transition is expected to occur [26], we observed (i) the SG transition accompanied by the critical slowing down of spin fluctuations, (ii) the form of relaxation changing from a Debye to a nonexponential form, and (iii) thermoremanent magnetization $M_{\rm TRM}(0)$ emerging rapidly. The presented comprehensive magnetic investigation for the random spinel magnet $CoGa_2O4$ might also provide insight for understanding magnetic properties for the frustrated antiferromagnet $CoAl_2O_4$ assigned to be in the vicinity of the NSS and NSG boundaries and facilitates further investigations.

ACKNOWLEDGMENTS

This work was partially supported by a Grant-in-Aid for Scientific Research, KAKENHI (Grants No. 25246013, No. 16K13999, No. 17H03404, and No. 20H01851) and the Research Institute for Science and Technology of Tokyo Denki University (Grant No. Q19K-02). The synchrotron radiation experiments were performed on the BL15XU beam line at SPring-8 with the approval of the Japan Synchrotron Radiation Research Institute (Grants No. 2015B4505, No. 2016B4505, and No. 2018A4507). The authors are grateful to Hiroaki Mamiya at the National Institute for Materials Science for valuable comments and suggestions on the ac-susceptibility measurement.

APPENDIX A: SPIN-GLASS TRANSITION AT $T_{\rm SG}$ AND CRITICAL EXPONENT $z\nu'$

As can be seen in Fig. 13, the relaxation time $\tau_{\rm ac}$ for $CoGa_2O_4$ shows a conventional power-law divergence of the critical slowing down at $T = T_{\rm SG}$,

$$\tau_{\rm ac}(T) = \tau_0 \left(\frac{T_f - T_{\rm SG}}{T_{\rm SG}} \right)^{-z\nu'}, \tag{A1}$$

where τ_0 is a characteristic relaxation time. Here we obtain $\tau_0 = 2.5(6)\times 10^{-10}$ s, $z\nu' = 9.8(1)$, and $T_{\rm SG} = 8.2$ K by the least squares method. The value of τ_0 corresponds well with that obtained above by the fitting to the VF law 2.86×10^{-10} s. The power exponent of $z\nu' = 9.8$ is comparable to the values in the range 4–12 found for canonical spin-glass systems [16]. Generally, the correlation length $\xi(T)$ diverges as $\sim (T - T_c)^{-\nu'}$, and the relaxation time as $\tau \sim \xi^z \sim (T - T_c)^{-z\nu'}$ when the temperature approaches the transition point, T_c.

APPENDIX B: NONEXPONENTIAL RELAXATION FUNCTIONS

The cluster of concern here is a microscopic and mesoscopic unit consisting of a large number of relaxing entities which can be characterized by its volume or relaxation time. The cluster volume is closely related to a coherence

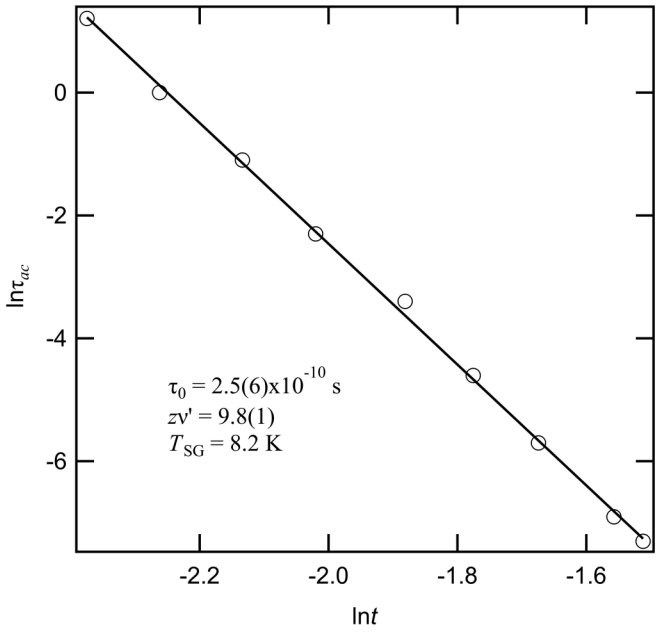

FIG. 13. Logarithmic plot of relaxation time τ_{ac} as a function of reduced temperature $t = (T_f - T_{SG})/T_{SG}$. Solid line represents the results of a least squares fit to the data.

length evaluated directly by microscopic probes, while relaxation time in a cluster is significantly different from its surroundings. Relaxation in glasses, which are typical complex physical systems, is a stochastic process that depends both on the geometric characteristics of the cluster, such as its morphology or fractal dimension, and on the collective nature of the interaction [28]. Generally, liquid and glass states are structurally quite similar. The most important and representative quantity between liquid and glassy states seems to be the degree of the relaxation time. In contrast with the logarithmic function $m_0 + S\ln(t)$ used generally for spin-glass systems, the following relaxation functions explicitly contain the relaxation time τ.

1. Kohlrausch (stretched exponential) function

The long-tail relaxation is well reproduced by the Kohlrausch (stretched exponential) form

$$\phi(t) = \exp\left[-\left(\frac{t}{\tau}\right)^{\beta}\right] \tag{B1}$$

for $0 < \beta < 1$. This function is asymptotically a logarithmic and Debye function at $\beta \to 0$ and 1, respectively.

2. Ogielski function

Monte Carlo calculations for a three-dimensional (3D) $\pm J$ Ising spin-glass model were conducted by Ogielski [58], who obtained the spin autocorrelation function of the spin-glass state. This function is phenomenologically expressed by

$$\phi(t) = t^{-x}\exp\left[-\left(\frac{t}{\tau}\right)^{\beta}\right], \tag{B2}$$

where the exponent x is in the range 0–0.5, and the relaxation time τ diverges at T_{SG}.

3. Weron's generalized probabilistic relaxation function

To describe dielectric relaxation consistent with experimentally established findings and based on purely stochastic theories, Weron proposed a universal relaxation function in a power-law form [24]:

$$\phi(t) = \left[1 + k\left(\frac{t}{\tau}\right)^{\beta}\right]^{-\frac{1}{k}} \tag{B3}$$

for $k > 0$ and $0 < \beta < 1$, where k and β are mathematical macroscopic parameters. The parameter k is called the interaction parameter and is related to the waiting time t_w, and "β represents macroscopically the 'fractal' geometry and dynamic nature of the relaxation dynamics" [28]. In the case of $k \to 0$, the stretched exponential form, Eq. (B1), is recovered. Later it was revealed that the dipolar relaxation function $\phi_{\gamma,q}(t)$ was derived for a cluster model based on the generalized maximum Tsallis nonextensive entropy principle [28], whereas it is assumed quite generally that the relaxation time τ of a volume v made of N relaxing elements scales as $\tau = v^{1/\gamma}$ with $0 < \gamma < 1$. The Tsallis generalized nonextensive entropy [26,27] is formulated as follows:

$$S_q = k_B \frac{1 - \int_0^{\infty} p^q(x)dx}{q - 1}. \tag{B4}$$

Equation (B4) consistently encloses the Boltzmann-Gibbs entropy $S_{BG} = -k_B \int_0^{\infty} p(x)\ln p(x)dx$ as an asymptotic form when the nonextensive parameter $q \to 1$. Here $p(x)$ is a distribution function in the sense of a probabilistic point of view, and x is, for example, a correlation length ξ in a dielectrically or magnetically correlated system or cluster volume v of an aggregated cluster system. Remarkably, asymptotic power laws of the response function $f_{\gamma,q}(t) = -\frac{d\phi_{\gamma,q}}{dt}$ obtained in both the limits $t \to 0$ and $t \to \infty$ are consistent

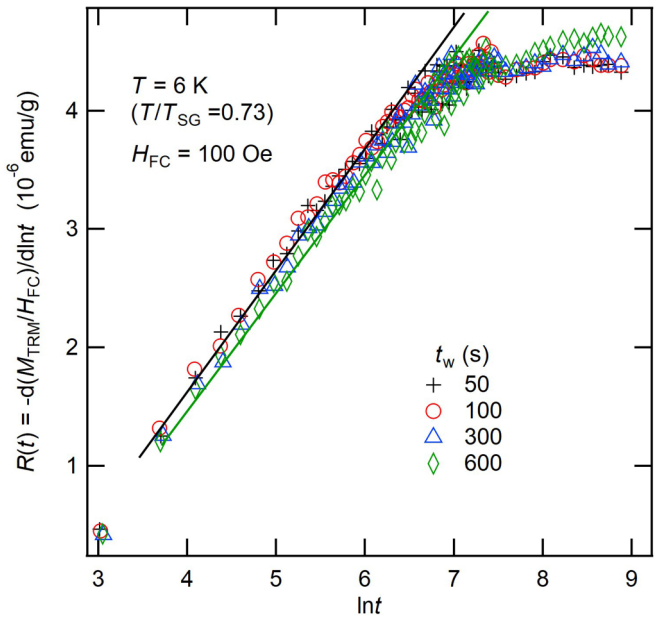

FIG. 14. Relaxation rate $R(t)$ as a function of logarithmic time ln$t$ at various waiting times. Solid line is a guide to facilitate visualization.

with those derived from the Weron function, Eq. (B3) [28]. This coincidence brings about a simple relation between the Tsallis parameter q in Eq. (B4) and the stochastic parameter k in Eq. (B3), i.e., $k = (q-1)/(2-q)$, in addition to $\beta = \gamma$. Moreover, it gives physical meanings to k and β, which were introduced as purely stochastic parameters by Weron [24].

APPENDIX C: EFFECTS OF AGING ON THE TRM RELAXATION CURVE

It is known in spin glasses [20,36] that the relaxation rate with respect to logarithmic time, which is defined as

$$R(t) = -d\left(\frac{M_{\mathrm{TRM}}}{H_{\mathrm{FC}}}\right)/d\ln t, \tag{C1}$$

exhibits a maximum at $t \sim t_{\mathrm{w}}$. The exhibition of this maximum is a kind of aging behavior. In $CoGa_2O_4$, however, $R(t)$ does not show a maximum, and there is some t_{w} dependence of $R(t)$, but the dependence is quite small in the range of $50 \leqslant t_{\mathrm{w}} \leqslant 600$ s (Fig. 14). In the TRM relaxation curves for $CoGa_2O_4$ taken after the waiting duration $t_{\mathrm{w}} = 300$ s, the fitting procedure and extracted parameters seem not to be seriously affected by aging effects.

[1] L. Savary and L. Balents, Rep. Prog. Phys. **80**, 016502 (2017).
[2] D. Bergman, J. Alicea, E. Gull, S. Trebst, and L. Balents, Nat. Phys. **3**, 487 (2007).
[3] K. W. Plumb, J. R. Morey, J. A. Rodriguez-Rivera, H. Wu, A. A. Podlesnyak, T. M. McQueen, and C. L. Broholm, Phys. Rev. X **6**, 041055 (2016).
[4] L. Bai, M. Pravica, Y. Zhao, C. Park, Y. Meng, S. V. Sinogeikin, and G. Shen, J. Phys.: Condens. Matter **24**, 435401 (2012).
[5] S. Hirai and W. L. Mao, Appl. Phys. Lett. **102**, 041912 (2013).
[6] K. Hanashima, Y. Kodama, D. Akahoshi, C. Kanadani, and T. Saito, J. Phys. Soc. Jpn. **82**, 024702 (2013).
[7] B. C. Melot, K. Page, R. Seshadri, E. M. Stoudenmire, L. Balents, D. L. Bergman, and T. Proffen, Phys. Rev. B **80**, 104420 (2009).
[8] T. Naka, K. Sato, Y. Matsushita, N. Terada, S. Ishii, T. Nakane, M. Taguchi, M. Nakayama, T. Hashishin, S. Ohara, S. Takami, and A. Matsushita, Phys. Rev. B **91**, 224412 (2015).
[9] T. Naka, J. Valenta, J. Kaštil, M. Míšek, J. Prchal, V. Sechovský, H. Abe, T. Nakane, M. Nakayama, and T. Uchikoshi, Mater. Res. Express **7**, 056105 (2020).
[10] L. Savary, E. Gull, S. Trebst, J. Alicea, D. Bergman, and L. Balents, Phys. Rev. B **84**, 064438 (2011).
[11] N. Tristan, J. Hemberger, A. Krimmel, H.-A. Krug von Nidda, V. Tsurkan, and A. Loidl, Phys. Rev. B **72**, 174404 (2005).
[12] T. Suzuki, H. Nagai, M. Nohara, and H. Takagi, J. Phys.: Condens. Matter **19**, 145265 (2007).
[13] G. J. MacDougall, D. Gout, J. L. Zarestky, G. Ehlers, A. Podlesnyak, M. A. McGuire, D. Mandrus, and S. E. Nagler, Proc. Natl. Acad. Sci. USA **108**, 15693 (2011).
[14] O. Zaharko, N. B. Christensen, A. Cervellino, V. Tsurkan, A. Maljuk, U. Stuhr, C. Niedermayer, F. Yokaichiya, D. N. Argyriou, M. Boehm, and A. Loidl, Phys. Rev. B **84**, 094403 (2011).
[15] B. Roy, A. Pandey, Q. Zhang, T. W. Heitmann, D. Vaknin, D. C. Johnston, and Y. Furukawa, Phys. Rev. B **88**, 174415 (2013).
[16] S. Ghara, N. V. Ter-Oganessian, and A. Sundaresan, Phys. Rev. B **95**, 094404 (2017).
[17] G. J. MacDougall, A. A. Aczel, Y. Su, W. Schweika, E. Faulhaber, A. Schneidewind, A. D. Christianson, J. L. Zarestky, H. D. Zhou, D. Mandrus, and S. E. Nagler, Phys. Rev. B **94**, 184422 (2016).
[18] O. Zaharko, S. Toth, O. Sendetskyi, A. Cervellino, A. Wolter-Giraud, T. Dey, A. Maljuk, and V. Tsurkan, Phys. Rev. B **90**, 134416 (2014).
[19] G. C. Papaefthymiou, Nano Today **4**, 438 (2009).
[20] S. Nair and A. K. Nigam, Phys. Rev. B **75**, 214415 (2007).
[21] J. L. Soubeyroux, D. Fiorani, and E. Agostinelli, J. Magn. Magn. Mater. **54–57**, 83 (1986).
[22] A. Nakatsuka, Y. Ikeda, N. Nakayama, and T. Mizota, Acta Crystallogr. **E62**, i109 (2006).
[23] F. Leccabue and C. Pelosi, J. Cryst. Growth **79**, 410 (1986).
[24] K. Weron, J. Phys. Condens. Matter **3**, 9151 (1991).
[25] R. M. Pickup, R. Cywinski, C. Pappas, B. Farago, and P. Fouquet, Phys. Rev. Lett. **102**, 097202 (2009).
[26] D. Prato and C. Tsallis, Phys. Rev. E **60**, 2398 (1999).
[27] C. Tsallis and E. Brigatti, Continuum Mech. Thermodyn. **16**, 223 (2004).
[28] F. Brouers and O. Sotolongo-Costa, Europhys. Lett. **62**, 808 (2003).
[29] F. Izumi and K. Momma, Solid. State Phenom. **130**, 15 (2007).
[30] E. Nishibori, M. Takata, K. Kato, M. Sakata, Y. Kubota, S. Aoyagi, Y. Kuroiwa, M. Yamakata, and N. Ikeda, Nucl. Instrum. Methods Phys. Res., Sect. A **467–468**, 1045 (2001).
[31] D. Fiorani and S. Viticoli, Solid State Commun. **25**, 155 (1978).
[32] V. K. Anand, D. T. Adroja, and A. D. Hillier, Phys. Rev. B **85**, 014418 (2012).
[33] J.-L. Tholence, Phys. B (Amseterdam, Neth.) **126**, 157 (1984).
[34] K. Binder and A. P. Young, Rev. Mod. Phys. **58**, 801 (1986).
[35] G. G. Kenning, Y. G. Joh, D. Chu, and R. Orbach, Phys. Rev. B **52**, 3479 (1995).
[36] G. G. Kenning, G. F. Rodriguez, and R. Orbach, arXiv:cond-mat/0402509.
[37] See for recent investigation and references contained herein: A. Kumar, A. Senyshyn, and D. Pandey, Phys. Rev. B **99**, 214425 (2019).
[38] A. Kumar and D. Pandey, J. Magn. Magn. Mater. **511**, 166964 (2020).
[39] T. Naka *et al.*, arXiv:1811.00186.
[40] V. Lubchenko and P. G. Wolynes, Annu. Rev. Phys. Chem. **58**, 235 (2007).
[41] S. López-Moreno, P. Rodróguez-Hernández, A. Muñoz, A. H. Romero, F. J.Manjón, D. Errandonea, E. Rusu, and V. V. Ursaki, Ann. Phys. (Berlin, Ger.) **523**, 157 (2011).
[42] G. G. P. Van Gorkom, J. H. Haanstra, and H. V. D. Boom, J. Raman Spectrosc. **1**, 513 (1973).
[43] T. Nakane, T. Naka, K. Sato, M. Taguchi, M. Nakayama, T. Mitsui, A. Matsushita, and T. Chikyow, Dalton Trans. **44**, 997 (2015).

[44] G. Busca, V. Lorenzelli, V. S. Escribano, and R. Guidetti, J. Catal. **131**, 167 (1991).
[45] M. Fabián, P. Bottke, V. Girman, A. Düvel, K. L. Da Silva, M. Wilkening, H. Hahn, P. Heitjans, and V. Šepelák, RSC Adv. **5**, 54321 (2014).
[46] A. A. Da Silva, A. de Souza Gonc, and M. R. Davolos, J. Sol-Gel Sci. Technol. **49**, 101 (2009).
[47] E. S. R. Gopal, *Specific Heats at Low Temperatures*, edited by K. Mendelssohn and K. D. Timmerhaus (Heywood Books, London, 1966).
[48] M. Bouvier, P. Lethuillier, and D. Schmitt, Phys. Rev. B **43**, 13137 (1991).
[49] C. M. Fang, C.-K. Loong, G. A. de Wijs, and G. de With, Phys. Rev. B **66**, 144301 (2002).
[50] J. O. Thomson and J. R. Thomson, J. Phys. F: Met. Phys. **11**, 247 (1981).
[51] A. Abragam and B. Bleaney, *Electron Paramagnetic Resonance of Transition Ions* (Clarendon, Oxford, 1970).
[52] L. G. Mamsurova, V. I. Sokolov, and E. M. Speranskaya, Zh. Eksp. Teor. Fiz. **69**, 666 (1975) [Sov. Phys. JETP **42**, 338 (1975)].
[53] E. A. Zvereva, M. I. Stratan, A. V. Ushakov, V. B. Nalbandyan, I. L. Shukaev, A. V. Silhanek, M. Abdel-Hafiez, S. V. Streltsov, and A. N. Vasiliev, Dalton Trans. **45**, 7373 (2016).
[54] F. Scholl and K. Binder, Z. Physik B - Condensed Matter **39**, 239 (1980).
[55] M. Bałanda, Acta Phys. Pol., A **124**, 964 (2013).
[56] N. Tristan, V. Zestrea, G. Behr, R. Klingeler, B. Büchner, H. A. Krug von Nidda, A. Loidl, and V. Tsurkan, Phys. Rev. B **77**, 094412 (2008).
[57] T. Mousavand, T. Naka, K. Sato, S. Ohara, M. Umetsu, S. Takami, T. Nakane, A. Matsushita, and T. Adschiri, Phys. Rev. B **79**, 144411 (2009).
[58] A. T. Ogielski, Phys. Rev. B **32**, 7384 (1985).

Correction: A minor typographical error in Eq. (4) has been fixed.